ACS SENSORS

Article

Cite This: ACS Sens. 2019, 4, 32–43

pubs.acs.org/acssensors

Implanted Nanosensors in Marine Organisms for Physiological Biologging: Design, Feasibility, and Species Variability

Michael A. Lee,[†] Freddy T. Nguyen,[†] Kathleen Scott,[‡] Nathan Y.L. Chan,[§] Naveed Ali Bakh,[†] Kelvin K. Jones,[†] Crystal Pham,[†] Pablo Garcia-Salinas,[∥] Daniel Garcia-Parraga,[∥] Andreas Fahlman,[∥] Vicente Marco,[∥] Volodymyr B. Koman,[†] Ronald J. Oliver,[†] Lloyd W. Hopkins,[⊥] Consuelo Rubio,[∥] Rory P. Wilson,[⊥] Mark G. Meekan,[#] Carlos M. Duarte,[¶] and Michael S. Strano*[,†]

[†]Department of Chemical Engineering and [§]Division of Comparative Medicine, Massachusetts Institute of Technology, Cambridge, Massachusetts 02139, United States

[‡]Office of Animal Resources, University of Iowa, Iowa City, Iowa 52242, United States

[∥]Fundación Oceanogràfic de la Comunitat Valenciana, Research Department, Ciudad de las Artes y las Ciencias, 46013 Valencia, Spain

[⊥]Biosciences, College of Science, Swansea University, Singleton Park, Swansea SA2 8PP, United Kingdom

[#]Australian Institute of Marine Science, the Indian Ocean Marine Research Centre (IOMRC), University of Western Australia Oceans Institute, 35 Stirling Highway, Crawley, Western Australia 6009, Australia

[¶]Red Sea Research Center, Division of Biological and Environmental Sciences and Engineering, King Abdullah University of Science and Technology, Thuwal 23955-6900, Saudi Arabia

Supporting Information

ABSTRACT: In recent decades, biologists have sought to tag animals with various sensors to study aspects of their behavior otherwise inaccessible from controlled laboratory experiments. Despite this, chemical information, both environmental and physiological, remains challenging to collect despite its tremendous potential to elucidate a wide range of animal behaviors. In this work, we explore the design, feasibility, and data collection constraints of implantable, near-infrared fluorescent nanosensors based on DNA-wrapped single-wall carbon nanotubes (SWNT) embedded within a biocompatible poly(ethylene glycol) diacrylate (PEGDA) hydrogel. These sensors are enabled by Corona Phase Molecular Recognition (CoPhMoRe) to provide selective chemical detection for marine organism biologging. Riboflavin, a key nutrient in oxidative phosphorylation, is utilized as a model analyte in *in vitro* and *ex vivo* tissue measurements. Nine species of bony fish, sharks, eels, and turtles were utilized on site at Oceanogràfic in Valencia, Spain to investigate sensor design parameters, including implantation depth, sensor imaging and detection limits, fluence, and stability, as well as acute and long-term biocompatibility. Hydrogels were implanted subcutaneously and imaged using a customized, field-portable Raspberry Pi camera system. Hydrogels could be detected up to depths of 7 mm in the skin and muscle tissue of deceased teleost fish (*Sparus aurata* and *Stenotomus chrysops*) and a deceased catshark (*Galeus melastomus*). The effects of tissue heterogeneity on hydrogel delivery and fluorescence visibility were explored, with darker tissues masking hydrogel fluorescence. Hydrogels were implanted into a living eastern river cooter (*Pseudemys concinna*), a European eel (*Anguilla anguilla*), and a second species of catshark (*Scyliorhinus stellaris*). The animals displayed no observable changes in movement and feeding patterns. Imaging by high-resolution ultrasound indicated no changes in tissue structure in the eel and catshark. In the turtle, some tissue reaction was detected upon dissection and histopathology. Analysis of movement patterns in sarasa comet goldfish (*Carassius auratus*) indicated that the hydrogel implants did not affect swimming patterns. Taken together, these results indicate that this implantable form factor is a promising technique for biologging using aquatic vertebrates with further development. Future work will tune the sensor detection range to the physiological range of riboflavin, develop strategies to normalize sensor signal to account for the optical heterogeneity of animal tissues, and design a flexible, wearable device incorporating optoelectronic components that will enable sensor measurements in moving animals. This work advances the application of nanosensors to organisms beyond the commonly used rodent and zebrafish models and is an important step toward the physiological biologging of aquatic organisms.

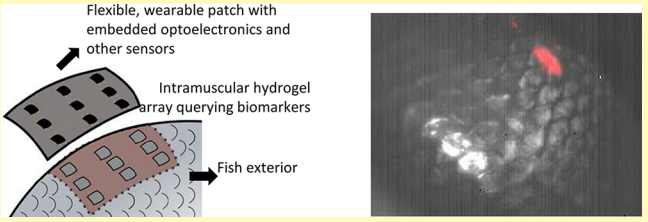

KEYWORDS: *SWNT, in vivo, biologging, aquatic organisms, hydrogel, sensor*

In recent decades, the biologging community has attached various types of sensors to animals to characterize animal behavior in the context of their environments.[1] These studies have produced key insights into a wide range of ecological

Received: June 22, 2018
Accepted: November 20, 2018
Published: December 11, 2018

DOI: 10.1021/acssensors.8b00538
ACS Sens. 2019, 4, 32–43

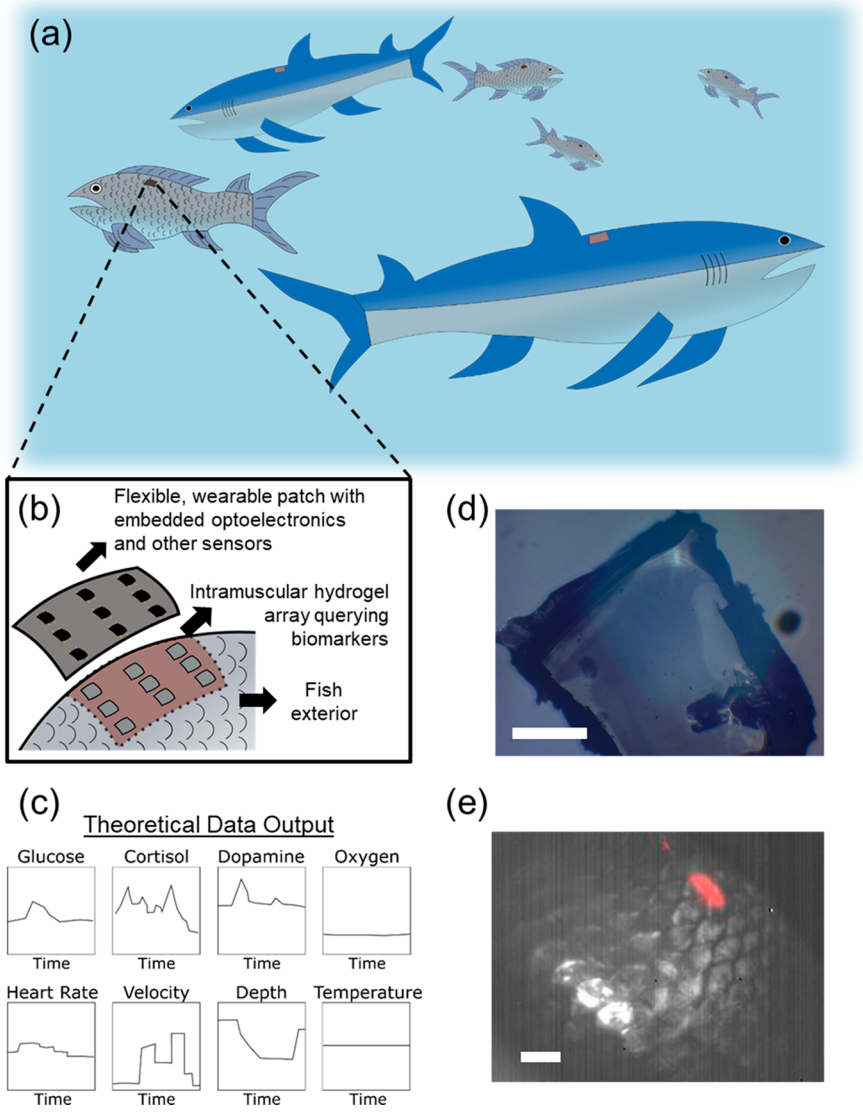

Figure 1. Vision for the future application of CoPhMoRe sensors to physiological biologging of marine organisms. (a) Animals of various sizes and ecological niches tagged with minimally invasive sensors collecting multivariate data sets continuously. (b) Theoretical design of a future biologging system. Hydrogel implants, encapsulating nanoparticles engineered to modulate their fluorescence in response to the local concentration of specific bioanalytes, are injected at a fixed depth in the intramuscular space, where they query biological fluid. Atop the fish's exterior is a flexible, wearable patch that contains embedded optoelectronics to excite and collect hydrogel fluorescence. The elastomer protects the electronic components from the surrounding aquatic environment, as well as conforming to the animal's movements. The device also incorporates other sensors to track animal movement and environmental conditions. The work herein describes the development of the hydrogel component of this theoretical device. (c) Theoretical data output of envisioned device. The device collects biochemical information and other animal-derived and environmental parameters such as velocity, depth, temperature, etc. (d) Visible image of SWNT-gels (scale = 0.5 mm). (e) Overlay of bright field image of sarasa comet goldfish (*Carassius auratus*) and fluorescence image of implanted hydrogel (scale = 10 mm).

phenomena, including the metabolic energy balance,[2] predator–prey relationships,[3] the ecological effects of climate change,[4] the impact of human activity on animals,[5] and other behaviors related to feeding,[6] migration,[7] and reproduction.[8] However, deployed sensors have largely been limited to environmental parameter sensors (temperature, pressure, and salinity), movement and location sensors (accelerometers and GPS), and vital sign sensors, such as heart rate monitors.[2] Notably missing from these tools are chemical sensors. These may be outward-facing, measuring analytes in the local environment around the animal, or inward-facing, measuring biochemical signaling pathways within the animal. The advent of novel technologies capable of real-time, continuous chemical sensing, such as those enabled by Corona Phase Molecular Recognition (CoPhMoRe), may enable access to this information and thereby significantly advance biologging studies.[9] Herein, we explore, for the first time, several design and operation issues associated with implantable sensors of this type for biologging applications, using near-infrared (nIR) fluorescent carbon nanotube sensors as a model for marine organisms to address aspects of feasibility. For this study and purpose, we have assembled a unique team of marine biologists, sensor developers, and engineers to address this challenge, as coauthors of this study.

Recent developments in *in vivo* sensing technologies offer tremendous opportunities for biologgers to probe the chemical network underpinning animal behaviors. As many excellent reviews have reported, *in vivo* sensors operating in several

DOI: 10.1021/acssensors.8b00538
ACS Sens. 2019, 4, 32−43

modalities—including optical and electrochemical—have been developed to measure a variety of biomarkers, including ions, reactive oxygen species, redox active molecules, oxygen, metals, and macromolecules, among many others.[10−18] Recently, Sun et al. measured glucose in mice using oxygen-sensitive polymer dots and a smartphone.[19] Measurements of hypochlorous acid and pH have been performed in zebrafish and their embryos.[20,21] Ferreira et al. modified carbon fiber microelectrodes and simultaneously measured ascorbate and glutamate in the hippocampi of anesthetized rats.[22] Despite these advances, the continuous glucose monitor remains one of the few technologies to be adopted due to stringent analytical and biocompatibility requirements for sensor integrity in *in vivo* environments.[13,14] Although biologically derived units such as antibodies, aptamers, and enzymes have traditionally been used for chemical sensing,[23] they may lose their capability for molecular recognition when conjugated to other sensor components and may also suffer from limited thermal and chemical stability, restricting their use *in vivo* to short periods of time.[24]

Synthetic sensing approaches have overcome some of these disadvantages. Our group has developed Corona Phase Molecular Recognition (CoPhMoRe), which uses a nIR fluorescent nanoparticle that acts as both the molecular recognition unit and the reporter of binding events.[9] An amphiphilic polymer or surfactant adsorbs onto singly dispersed single-wall carbon nanotubes (SWNT) via hydrophobic interactions. The hydrophilic groups on the polymer provide the dispersion colloidal stability in aqueous solutions, where a majority of bioanalytes exist. The conformation of the adsorbed phase, or the corona, modulates analyte binding to the nanoparticle and provides selectivity. Upon analyte binding, the fluorescence intensity and/or peak wavelength may change. To date, CoPhMoRe sensors have been fabricated for a variety of molecules, including nitric oxide,[25] hydrogen peroxide,[26] riboflavin, L-thyroxine, estradiol,[9] dopamine,[27,28] fibrinogen,[24] and insulin.[29] The nitric oxide sensor has been demonstrated *in vivo* and shown to have a fluorescence stability of over 400 days within the body of a mouse.[30]

The challenge facing researchers is to now incorporate these new types of physiological sensors into biologging devices.[31] In the past, the biologging community has traditionally focused on sensors that describe the behaviors, external environments, and location of animals. Accelerometers, depth, and temperature sensors and Argos satellite-linked and GPS tags have been central to this task.[32] For example, using accelerometers, Wilson et al. studied the significance of neck length in swimming and foraging behaviors in Imperial cormorants and Megallanic penguins,[33] Hays et al. used records from satellite tagging of thousands of sea turtles to compare their migration distances with those of other similarly sized marine animals,[7] and Meekan et al. used a combination of an accelerometer, magnetometer, GPS, and depth sensors to study the energy efficiency of whale shark movement patterns.[34]

The combination of sensors that collect data sets of movement, location, and relevant biochemical parameters (such as glucose, dopamine, and cortisol)[28,29,35] into biologging tags potentially offers unprecedented insights into the behavior, ecology, and condition of animals. To date, physiological data in biologging tags has mostly been obtained from electromyogram (EMG) and heart rate sensors.[2] Although there have been a few examples of bioanalyte measurements in extracted blood,[36−38] the measurement of biomarkers in sampled fluid *ex vivo* offers limited information and may introduce artifacts due to the capture and restraint of the animal.[35] CoPhMoRe sensors incorporated into animal-borne sensor tags have the potential to transform biologging studies by giving researchers continuous and real-time access to biomarkers reflecting the condition of free-living animals (Figure 1).[39,40]

In this work, as a model sensor implant, we use DNA-wrapped SWNT that we have fabricated and encapsulated into a biocompatible poly(ethylene glycol) diacrylate (PEGDA) hydrogel and calibrated against riboflavin, an essential nutrient involved in oxidative phosphorylation.[41] *In vitro* characterization and experiments with two species of aquatic organisms were performed at MIT, whereas experiments with an additional seven species were performed at Oceanogràfic in Valencia, Spain from January 30 to February 1, 2018. The implants were delivered via trocar to both recently deceased and living animals. The hydrogel detection limit with injection depth was determined, and the effects of tissue heterogeneity on fluorescence detection were explored. The three living animals showed no external signs of adverse health or behavioral changes one month after implantation. However, in the case of the turtle, some tissue reaction was detected upon dissection and histopathology. At MIT, analysis of goldfish swimming patterns indicated that the hydrogel implants do not impair animal movement. All together, these data indicate the feasibility of using CoPhMoRe sensors for marine organism biologging with further improvements to sensor detection limits, normalization of sensor signal to account for individual tissue optical properties, and wearable fluorescence device design.

METHODS AND MATERIALS

Materials. (6,5)-Enriched SWNTs produced by the CoMoCAT process (lot # MKBZ1159 V) were purchased from Sigma-Aldrich. Single-stranded $(AC)_{15}$ was purchased from Integrated DNA Technologies, while PEGDA (M_n = 8000) was purchased from Alfa Aesar. Unless otherwise noted, other reagents were purchased from Sigma-Aldrich.

Sensor Fabrication. SWNT (1 mg/mL) and ss$(AC)_{15}$ (2 mg/mL) were mixed in 2 mL of 100 mM sodium chloride. The mixture was bath sonicated for 10 min, followed by sonication with a 3 mm probe at 4 W for 20 min (QSonica). The suspension was centrifuged at 32,000 rcf for 3 h, and the top 80% of the supernatant was collected for further use. Free DNA was removed using 100 kDa MWCO centrifugal filters (Merck Millipore) with 5 volumetric replacements with 1× phosphate buffered saline (PBS). UV−vis-NIR absorption spectra were collected to verify successful suspension. The SWNT mass concentration was calculated using the absorption value at 632 nm.

ssDNA-SWNT (0.1 mg/mL), PEGDA (100 mg/mL), and 2-hydroxy-4′-(2-hydroxyethoxy)-2-methylpropiophenone (0.175 mg/mL) were mixed in 1× PBS, cast into glass molds, and incubated for 30 min under a nitrogen atmosphere. The samples were then illuminated under 365 nm ultraviolet radiation (UVP Blak-Ray XX-15BLB, 15 W) for 60 min. The hydrogels were removed from the molds and incubated in excess 1× PBS for 48 h to remove unreacted monomers and unencapsulated SWNT. The hydrogels were then incubated in fresh 1× PBS until further use.

***In Vitro* Characterization.** UV−vis-NIR absorption spectra were measured for both solution phase and hydrogel encapsulated ssDNA-SWNT (Shimadzu UV-3101PC). Fluorescence spectra were measured in a custom-built NIR microscope. Samples were illuminated using a 785 nm photodiode laser (B&W Tek. Inc.) and imaged using a Zeiss AxioVision inverted microscope with appropriate optical filters. The fluorescence was passed through a Princeton Instruments Acton SP2500 spectrometer and measured using a liquid nitrogen cooled Princeton Instruments InGaAs 1D detector.

Riboflavin was used as a model analyte to test hydrogel chemical sensitivity *in vitro* and *ex vivo*. Hydrogels were cut into 5 × 5 × 1 mm^3

DOI: 10.1021/acssensors.8b00538
ACS Sens. 2019, 4, 32−43

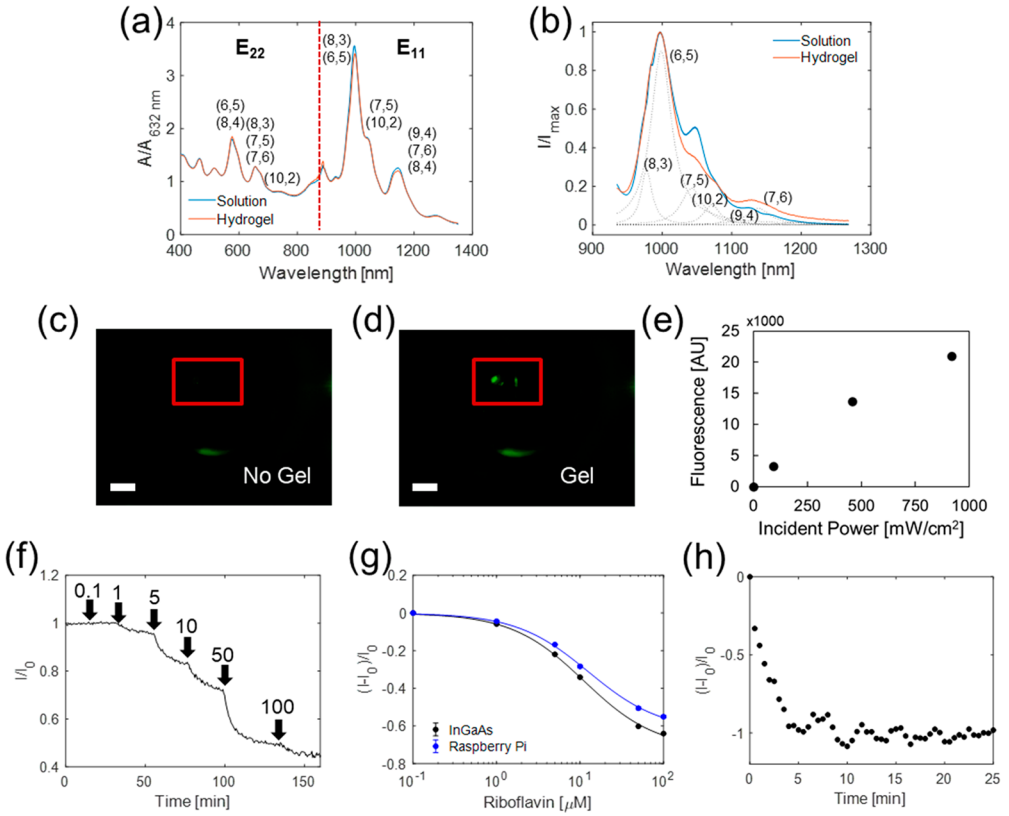

Figure 2. *In vitro* and *ex vivo* sensor characterization. (a) Normalized UV−vis-NIR absorption spectra and (b) fluorescence emission spectrum at 785 nm excitation of of ss$(AC)_{15}$-wrapped (6,5) CoMoCAT SWNT. Spectra were measured for solution phase SWNT and SWNT-gels. The absorption spectrum shows both the excitation (E_{22}) and fluorescence emission peaks (E_{11}) for the corresponding SWNT chiralities given in parentheses. The fluorescence spectrum was decomposed into individual peaks corresponding to the labeled SWNT chiralities. (c,d) Images taken with Raspberry Pi imaging setup (c) without and (d) with a SWNT-gel. (e) Hydrogel fluorescence increased with larger incident excitation power. (f) Fluorescence decreased with stepwise increases in riboflavin concentration between 1 to 100 μM, as measured by a Raspberry Pi camera. (g) Riboflavin calibration curves obtained with an InGaAs camera and the Raspberry Pi camera show good agreement. (h) SWNT-gel response to bolus injection of 100 μM riboflavin while placed 1 mm deep into *ex vivo* tissue sample of *Stenotomus chrysops*. The fluorescence decreased below the limit of detection of the Raspberry Pi camera.

sections and placed inside perfusion channels (ibidi μ-Slide III 3D Perfusion). Hydrogel fluorescence was monitored while varying the concentration of riboflavin in 1× PBS between 0−100 μM at a flow rate of 0.3 mL/min. Fluorescence images were taken using a liquid nitrogen cooled Princeton Instruments InGaAs 2D detector. These measurements were also performed on a 5 × 5 × 2 mm^3 section of hydrogel placed 1 mm below the surface of skin and muscle tissue of *Stenotomus chrysops*. A 500 μL bolus of 100 μM riboflavin was introduced atop of the hydrogel.

***In Vivo* Implantation.** All procedures described below were approved by the animal ethics committee of the Fundación Oceanogràfic de la Comunitat Valenciana (OCE-10-18) and performed at Oceanogràfic over the duration of the experiments.

Prior to implantation, hydrogels were illuminated by UV light for 15 min and handled in a biological hood (Telstar AV-100) thereafter to ensure sterility. Hydrogels were cut to a 1 × 5 × 1 mm^3 block and loaded into 12 gauge transponder needles from which the microchips were removed (Avid Suds Monoject).

The implantation procedure varied depending on the target organism. In the case of deceased animals, all animals were injected without further treatment of the skin. Hydrogels were placed at the desired location and penetration depth by using the needle length and angle of insertion as a guide.

A live European eel (*Anguilla anguilla*) was anesthetized prior to injection by submersion in a 70 mg/L benzocaine solution. When the eel was nonresponsive, the injection site on the dorsal side was washed with sterile saline, and the hydrogel was injected. The eel was moved to new water and allowed to recover prior to further handling.

A live eastern river cooter (*Pseudemys concinna*) and catshark (*Scyliorhinus stellaris*) were restrained by animal care personnel for hydrogel implantations. The skin of the shark was washed with sterile saline, whereas the skin of the turtle was disinfected with iodopovidone. The hydrogel was injected subcutaneously in the dorsal area of the shark at the level of the second dorsal fin and in the dorsal part of the cranial tram of the turtle's neck.

After implantation, the animals were monitored for 2 months to determine tolerance to the implants and changes in swimming and feeding behavior. High-resolution ultrasound images of the implantation site were used to noninvasively study the impacts of implantation on tissues. After one month, the turtle was euthanized (for reasons not related to this study), allowing biopsies of the implantation site to be collected for histopathology.

Imaging Using Raspberry Pi. The imaging system consisted of a Raspberry Pi 3 (Adafruit) with a 5 MP camera with the IR filter removed (SainSmart). The camera was placed inside of a 1 in. lens tube. The camera was used without further modification when taking brightfield images. The Picamera software package was used to control the camera.

When taking fluorescence images, the hydrogels were illuminated with a 200 mW 561 nm laser (Opto Engine LLC) passing through a collimator. Fluorescence passed through a 900 long-pass filter prior to collection by the camera. Fluorescence was quantified by taking two images before and after hydrogel placement and calculating the difference in gray value in the region of interest. For all images, the autowhite balance gains, exposure times, and shutter speed were set

DOI: 10.1021/acssensors.8b00538
ACS Sens. 2019, 4, 32−43

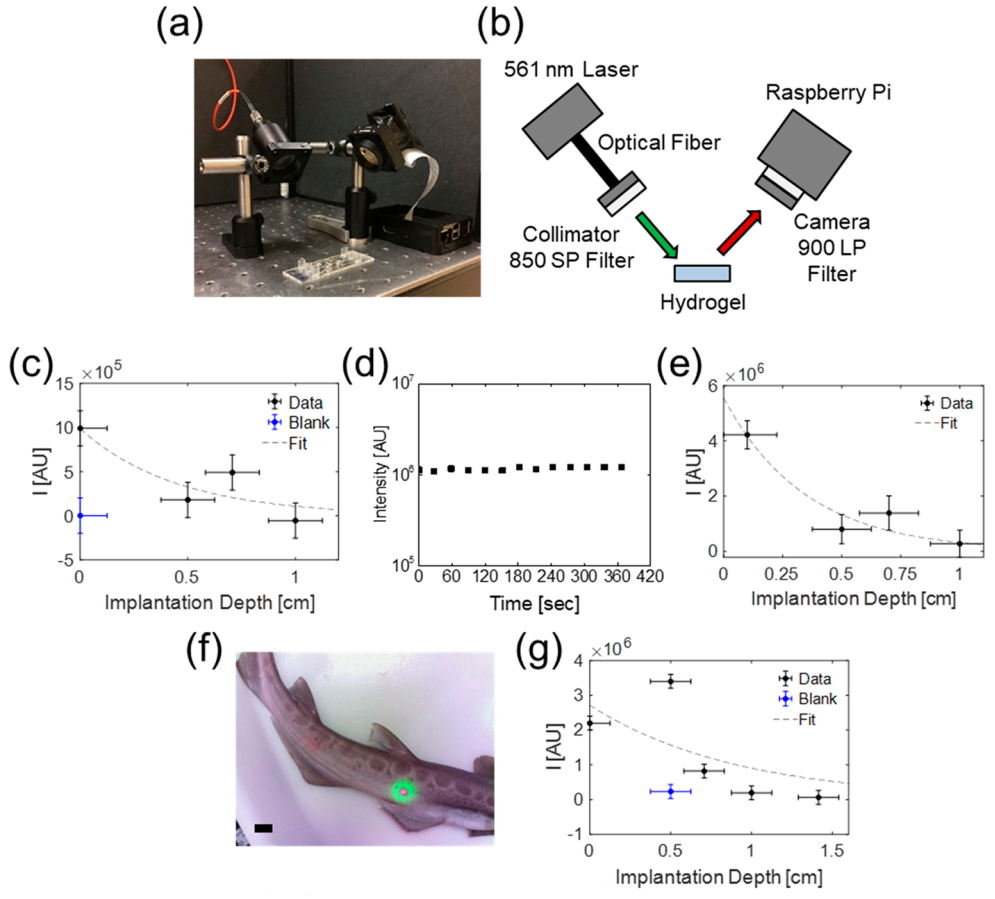

Figure 3. Effect of hydrogel implantation depth on fluorescence detection in teleosts (*Sparus aurata* and *Stenotomus chrysops*) and cat shark (*Galeus melastomus*). (a,b) Imaging setup and schematic. A fiber-coupled 561 nm laser fitted with an 850 short-pass filter was used to illuminate the implantation site before and after intramuscular delivery of hydrogels into previously deceased animals via trocar. The signal was collected by a Raspberry Pi camera connected to a 900 long-pass filter. The difference in gray values with and without the hydrogel was calculated. (c) In *Sparus aurata*, detectable hydrogel fluorescence decreased as injection depth was increased from just below the skin down to a limit of 0.7 cm. A nonfluorescent hydrogel was injected just superficially below the skin and imaged to give the threshold difference in intensity for the signal to be attributable to the hydrogel and not to other artifacts, such as movement of the fish relative to the laser. (d) A superficially implanted SWNT-gel in *Sparus aurata* exhibited a steady fluorescence signal when imaged over 6 min. (e) The detection limit of SWNT-gels in *Stenotomus chrysops* was 0.7 cm. (f) Overlay of brightfield and fluorescence images of a fluorescent hydrogel implanted 0.5 cm below the skin in *Galeus melastomus* [scale = 20 mm]. (g) SWNT-gels were detected down to a depth of 0.7 cm in *Galeus melastomus*, as compared to a nonfluorescent hydrogel implanted at a depth of 0.5 cm.

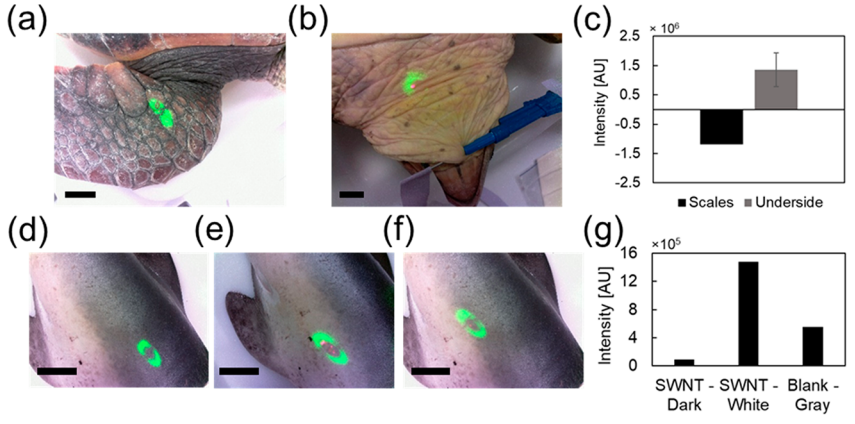

Figure 4. Detection of fluorescent hydrogels implanted superficially in optically heterogeneous tissues. Fluorescent hydrogels were implanted into (a) the scaly legs and (b) softer flesh beneath the neck of a sea turtle (*Caretta caretta*) (scale = 20 mm). (c) Hydrogel fluorescence was detected in the neck but not the scaly legs. SWNT-gels were implanted subcutaneously in (d) dark and (e) white regions of a blue shark (*Prionace glauca*). A nonfluorescent hydrogel was implanted in (f) gray region of the tissue. (g) Fluorescence could be detected underneath white skin but not dark skin. The blank hydrogel in the gray region provided a baseline against which to determine fluorescence detection. Scale in all images is 20 mm.

DOI: 10.1021/acssensors.8b00538
ACS Sens. 2019, 4, 32−43

manually. The analog and digital gains were kept constant by equilibration of the camera for a 1 min period.

Goldfish Hydrogel Implantations and Motion Tracking. All experimental details below and associated husbandry procedures were reviewed and approved by the Committee on Animal Care at MIT.

Two sarasa comet goldfish (*Carassius auratus*) were purchased from LiveAquaria, housed in a 110 L glass aquarium with dimensions of 76 × 42 × 30 cm^3 (length × width × height), and allowed to acclimate for at least 2 weeks prior to experimental manipulation. The water was maintained at 24 °C, and the aquarium was lit daily for 10 h. Fish were fed daily with flake foods (TetraFin).

Prior to implantation, hydrogels were treated under UV light for 15 min and handled in a biological hood thereafter to ensure sterility. Hydrogels were cut to a 1 × 3 × 1 mm^3 shape and loaded into 16 gauge needles. Fish were anesthetized in a solution of 60 mg/L tricaine methanesulfonate. When the fish were nonresponsive to handling and a fin pinch, the hydrogels were injected into muscle just below the dorsal fin. The fish were allowed to recover in a holding tank before being returned to the home tank.

To determine the impact of the hydrogel implant on the animal's health, its movements were recorded using a surveillance system consisting of the Raspberry Pi 2 computer with a Raspberry Pi Camera Board v2. Fish movements were extracted using the Kinovea software.

After the experimental lifetime, the fish were euthanized by submersion into a 500 mg/L solution of tricaine methanesulfonate.

RESULTS AND DISCUSSION

Sensor Fabrication and *in Vitro* Optical Characterization. DNA-wrapped SWNT have been utilized in many studies due to their high wrapping efficiency[42,43] and flexibility in selective sensing of different analytes.[25−27,30,44] The UV−vis-NIR absorption spectrum (Figure 2a) shows distinct peaks, indicating successful nanoparticle suspension. Mass concentration of total carbon in the solution was estimated using an extinction coefficient of $\varepsilon_{632\ nm} = 0.036\ (mg/L)^{-1}\ cm^{-1}$.[45] Singly dispersed ss$(AC)_{15}$-SWNT nanoparticles were produced at a 36% yield based on a carbon mass balance.

Peak position and relative peak intensities of ss$(AC)_{15}$-SWNT in solution phase or encapsulated in the hydrogel (SWNT-gel) were identical in both the absorption spectra and fluorescence emission spectra (Figure 2b), indicating that the dielectric environments surrounding the SWNT were nearly identical.[46,47] The absorption spectrum of the SWNT-gel indicated a final concentration of 33 mg/L SWNT. However, the fluorescence intensity of the SWNT-gel was only 50% of the intensity in the equivalent concentration in solution phase. Sample geometry contributed to this decrease, as the hydrogels are only 1 mm in thickness, whereas liquid samples were typically 1 cm in height. Additionally, the chemical environment of the sensors in the hydrogel is different, in that the SWNT are diffusionally constrained by a polymer matrix. Free radicals that are generated during the photopolymerization of the hydrogel may have also chemically altered the DNA on the SWNT surface.

Characterization of SWNT-Gel Pore Size. The hydrogel pore size formed by the spacing between cross-linked polymer chains is a critical parameter that controls sensor functionality and environment. The pores in the gel determine the size of the analyte that is permitted to enter the network, as well as its rate of diffusion, thereby affecting sensor response time.[48] The pore size can also be used to exclude large molecular weight interfering molecules to improve sensor selectivity. Furthermore, the hydrogel's pore diameter relative to nanoparticle size dictates the degree of nanoparticle entrapment.[49]

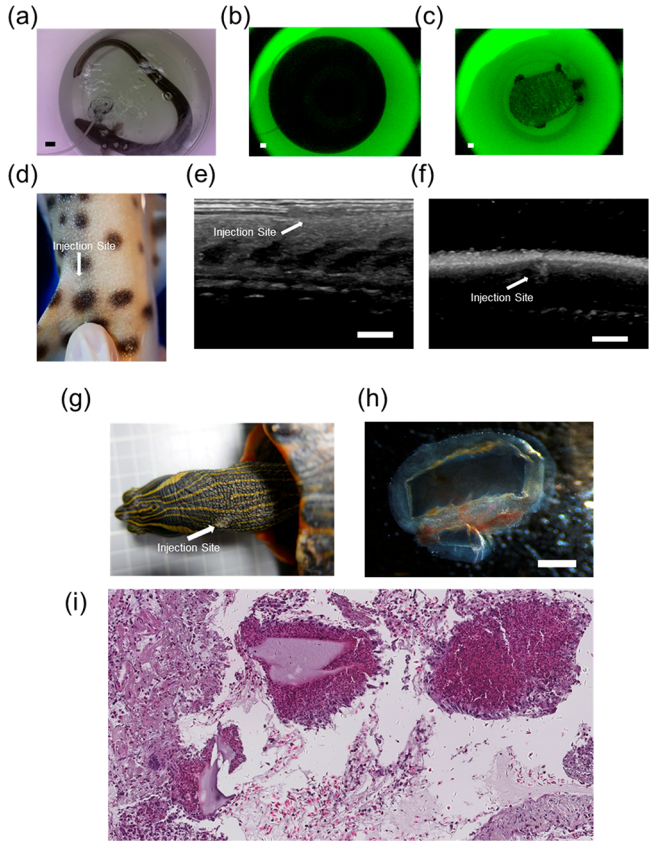

Figure 5. NIR fluorescent hydrogels implanted in a living European eel (*Anguilla anguilla*), eastern river cooter (*Pseudemmys concinna*), and catshark (*Scyliorhinus stellaris*). (a) Following implantation, attempts were made to track the fluorescence in the eel and turtle confined to a small space. (b,c) Dispersed laser excitation, animal movement, and long exposure times made these attempts unsuccessful in (b) the eel and (c) the turtle. All scalebars are 20 mm. (d) The implantation site fully healed in the catshark by 33 days post-implantation. (e,f) High resolution ultrasound images were taken to examine noninvasively tissue response to the implant 4 weeks after implantation in the (e) eel and (f) catshark (scale = 5 mm). The absence of significant changes in tissue architecture and echogenicity indicates that the hydrogels were well-tolerated in these organisms. (g) The injection site in the turtle did not heal completely 33 days post-implantation. (h) Hydrogels were removed from the turtle after 33 days and were found to be encapsulated by tissue. (i) Histology images from subcutaneous tissue surrounding the hydrogel implant in the turtle indicate a foreign body tissue reaction (Image courtesy of Pathology Service, UCH-CEU Valencia).

Swelling experiments were performed in 1× PBS to obtain the average SWNT-gel pore size from the polymer network. The swelling ratio was determined using the following equation

$$Q = \frac{m_{swollen}}{m_{dry}} = \alpha^{-1} \tag{1}$$

where Q is the hydrogel swelling ratio and m is the hydrogel mass. Q can then be used to calculate the average pore diameter:[50,51]

$$\bar{M}_c^{-1} = \frac{2}{\bar{M}_n} - \frac{(\bar{v}/V_2)[\ln(1-\alpha) + \alpha + \chi\alpha^2]}{\alpha^{1/3} - (2/\theta)\alpha} \tag{2}$$

DOI: 10.1021/acssensors.8b00538
ACS Sens. 2019, 4, 32−43

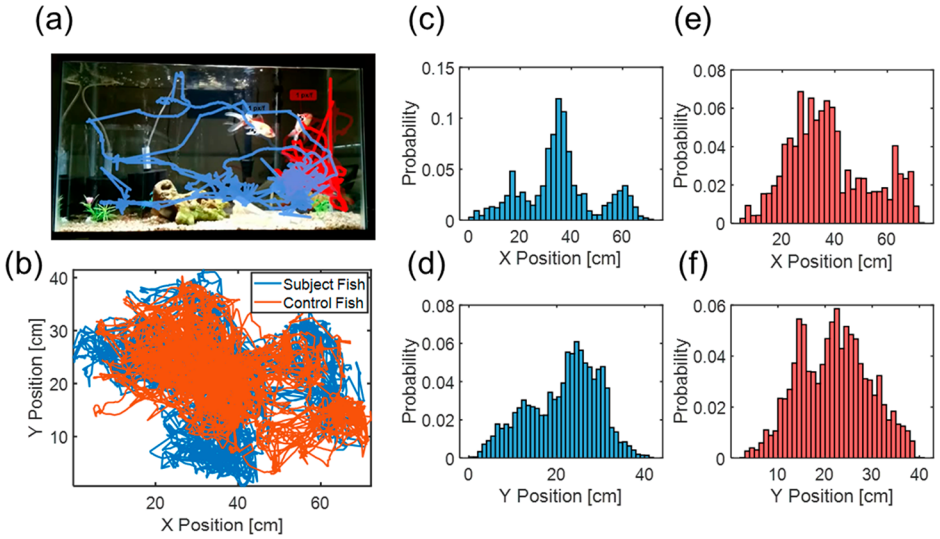

Figure 6. Quantification of hydrogel implant impact on animal health. (a) Snapshot of the capture video with corresponding sarasa comet goldfish (*Carassius auratus*) movement trajectories included. Blue corresponds to a fish in which a nIR fluorescent hydrogel was implanted, while orange corresponds to a control fish without a hydrogel implant. (b) Trajectories of fish taken for 1 h 2 days after a hydrogel was implanted into the subject fish. (c–f) *X* and *Y* position histograms for the subject fish (c,d) and control fish (e,f). The subject fish experienced neither impaired movement nor erratic movement due to the hydrogel implant, indicating good tolerance of the implant.

$$\zeta = \alpha^{-1/3}\left(\frac{2C_\infty l^2 \bar{M}_c}{M_0}\right)^{1/2} \tag{3}$$

where $\bar{M}_C$ is the molecular weight between cross-links, $\bar{M}_n$ is the molecular weight of the polymers without cross-linking (=8000), $\bar{v}$ is the specific volume of the polymer (= 0.903 mL/g), V_2 is the specific volume of water (= 18.01 mL/mol), χ is the Flory–Huggins parameter (= 0.3765), θ is the functionality of PEGDA (= 4), ξ is the average mesh side, C_∞ is the Flory characteristic ratio (= 6.9), l is the carbon–carbon bond length (= 0.154 nm), and M_0 is the molar mass of the repeat unit (= 44.05 g/mol). The Flory parameter was obtained from a previous study of PEG polymers.[52] The average pore size was estimated to be 15 nm.

Raspberry Pi Imaging Systems. To understand the range of organism–environment interactions and document variation among individuals and populations, some biologging studies have deployed sensors on anywhere from dozens to hundreds of animals.[7,53] To this end, some laboratory instruments are not practical due to their prohibitive cost for large-scale deployment, immobility, and fragility on a moving animal in its natural environment. For example, InGaAs cameras typically used to measure near-infrared fluorophores can weigh on the order of 5 kg and can cost thousands of dollars.[9,24,29] Consequently, we chose to use inexpensive and portable Raspberry Pi computers and cameras which cost on the order of tens of dollars. In the real application, the components of a Raspberry Pi imaging system can be readily incorporated into a miniaturized sensor suite. Recently, Görögcs et al. incorporated a similar CMOS image sensor into a portable imaging device weighing less than 40 g.[54]

Because the optical sensors on the cameras are fabricated from silicon, which have limited sensitivity (<0.1 A/W above 980 nm) to the near-infrared fluorescence of SWNT (Figure S-1), we first verified that the hydrogels could be visualized by our system (Figure 2c,d). Analysis showed a linear trend of hydrogel fluorescence with incident laser power density (Figure 2e).

Riboflavin as a Model Analyte for Chemical Sensing *in Vitro* and *ex Vivo*. Riboflavin plays a key role in the recycling of FADH and FAD^+ in oxidative phosphorylation and is an essential nutrient in a fish's diet.[41,55] Riboflavin exists in plasma typically between 1 and 100 nM.[56,57] Furthermore, DNA oligonucleotides of various sequences, when complexed to SWNTs, allow for a nIR fluorescence modulation in response to riboflavin binding via both intensity quenching and wavelength shifts,[9] making it an ideal model analyte to evaluate *in vivo* sensing feasibility.

The SWNT-gels showed stepwise decreases in fluorescence with stepwise increases in surrounding riboflavin concentration, with sensitivity from 1 to 100 μM (Figure 2f). The calibration curves were fitted to the following functional form:

$$\text{Response} = \frac{I - I_0}{I_0} = \beta\frac{C}{C + K_D} \tag{4}$$

where β is the gain, C is the riboflavin concentration, and K_D is the equilibrium dissociation constant. To evaluate the performance of the Raspberry Pi relative to typical laboratory equipment, we compared results obtained with a Princeton Instrument 2D InGaAs camera. The calibration curves showed good agreement (Figure 2g). For the InGaAs camera, β was −0.72, and K_D was 11.3 μM, while the corresponding values were −0.63 and 12.7 μM for the Raspberry Pi. The difference in maximum response is a product of higher background signal in the Raspberry Pi, which partially masked the fluorescence quenching of the riboflavin. Future versions of the sensor tag will be designed to eliminate such interference by optimizing optical configurations and increase the sensitivity to detect physiological levels of riboflavin.

Furthermore, the fluorescence of the SWNT-gels decreased in response to a bolus of 100 μM when placed in a 1-mm-thick skin and muscle tissue sample of *Stenotomus chrysops* (Figure 2h). The fluorescence decreased below the detection limit of the Raspberry Pi camera.

Optical Penetration Depth. We constructed a simplified, 1-D mathematical model to describe the effects of material, tissue, and equipment properties on the optical signal from a

DOI: 10.1021/acssensors.8b00538
ACS Sens. 2019, 4, 32–43

sensor implanted into tissue. Incident excitation light is partially reflected from the epidermal interface

$$I_0 = I_i(1 - r_{ex}) \tag{5}$$

where I_i and I_0 are the incident and transmitted excitation fluences, respectively, and r_{ex} is the epidermal reflectivity at the excitation wavelength. Tissue further attenuates excitation light according to the Beer−Lambert law

$$\log\left(\frac{I_0}{I}\right) = \gamma_{ex} d \tag{6}$$

where I is the fluence at the implantation site, γ_{ex} is the tissue extinction coefficient at the excitation wavelength, and d is distance through tissue. The fluorescence intensity of the hydrogel at the implantation site is described by

$$\log\left(1 - \frac{F_0}{\eta I A}\right) = -\epsilon_{ex} c t \tag{7}$$

where F_0 is the fluorescence intensity at the implantation site, η is the quantum efficiency of SWNT, A is the cross-sectional area of the hydrogel, ε_{ex} is the extinction coefficient of SWNT at the excitation wavelength, c is the concentration of SWNT in the hydrogel, and t is the hydrogel thickness. The thickness of the hydrogel is assumed to be negligible compared to the implantation depth. The fluorescence reaching the surface of the epidermis is given by the following equation

$$\log\left(\frac{F_0}{F}\right) = \gamma_{em} d \tag{8}$$

where F is the fluorescence reaching the epidermal interface, γ_{em} is the tissue extinction coefficient at the emission wavelength. Back-reflection of fluorescence may occur at the epidermal interface

$$F_f = F(1 - r_{em}) \tag{9}$$

where F_f is the fluorescence exiting the tissue and r_{em} is the reflectivity at the fluorescent wavelength. Assuming minimal scattering and absorption between the epidermal surface and the photodetector, the measured signal is described by

$$S = F_f R \tag{10}$$

where S is the signal, and R is the responsivity of the camera. Combining eqs 5−10 yields

$$\log\left(\frac{S}{\eta A R I_i (1 - r_{ex})(1 - r_{em})}\right) = \log(1 - 10^{\varepsilon_{ex} c t}) - d(\gamma_{ex} + \gamma_{em}) \tag{11}$$

The terms in eq 11 can be classified into material, tissue, and equipment properties and tunable engineering parameters. The specific fluorophore dictates the value of η and ε_{ex}. Different tissues attenuate light transmission to varying extents and consequently have unique values of γ, which may be measured in a future study via light transmission measurements. Both absorption and scattering contribute to the extinction coefficient. Scattering decreases with increasing incident wavelength,[58] while absorption is largely determined by water and blood absorption, which is minimal in the SWNT fluorescent region.[59] Furthermore, unlike organic fluorophores, SWNT do not photobleach and thus exhibit a constant c as long as the implant maintains its integrity. Thus, the near-infrared fluorescence of SWNT is ideal for an *in vivo* optical biosensor due to the lack of photobleaching and the transparency of the near-infrared window.[60,61] Controllable parameters include I_i, A, c, t, r, and d. Increased hydrogel thickness, fluorophore concentration, equipment responsivity, and excitation power and decreased implantation depth increase the fluorescence signal. In a previous study, Iverson et al. measured the fluorescence of an alginate hydrogel with 10 mg/L SWNT to a depth of 5 mm in tissue phantoms using a hyperspectral CRI Maestro system.[62]

For this application, consideration of the marine organism tissue properties is critical. Many fish species, including teleosts, have evolved skin containing significant amounts of reflective guanine crystals in the stratum argenteum and underneath the scales, which may camouflage the animal against predators.[63] The reflective spectra of such biomaterials have been thoroughly characterized in previous work.[64] These different skin types will affect the penetration of light through tissue. Others, such as sharks and marine reptiles, have evolved thick, mechanically stiff skin and/or scales as protection against environmental hazards, which may require specialized methods of placing implantable devices.[65] All together, these factors suggest that each species should be considered individually when using implantable nIR fluorescent hydrogel sensors for biologging.

Two deceased teleosts (*Sparus aurata* and *Stenotomus chrysops*), a female adult catshark (*Galeus melastormus*) were used for the nIR penetration versus depth study. The teleosts were chosen because over 32,500 species exist, making them the largest category of vertebrates.[66] Furthermore, catsharks comprise over 10% of extant cartilaginous fish.[67] Images were taken of the fish before and after placement of the hydrogel using the Raspbery Pi camera system (Figure 3a,b). Movement of the animal relative to the imaging setup was minimized such that differences in signal between the two images is predominantly the hydrogel, not position change. In *Sparus aurata*, the nIR fluorescent SWNT-gels were detected up to a depth of 7 mm (Figure 3c). Injection of sham nonfluorescent hydrogels using the same method verified that the difference in signal due to movement was negligible compared to the additional signal from the fluorescence. The residual signal is a small change in laser reflection from a small shift in position of the fish tissue. The SWNT-gels also exhibited stable fluorescence (Figure 3d). This stability is critical, so that perturbations can be attributed solely to changes in analyte concentrations. For *Stenotomus chrysops* and *Galeus melastormus* (Figure 3e−g), the SWNT-gels were detected again to a depth of 7 mm over a minimum signal difference threshold determined by injection of a nonfluorescent hydrogel (Figure 3g). A simplified version of eq 11 was used to fit the data and reproduced the trends.

$$S = a \cdot 10^{b \cdot d + c} \tag{12}$$

The fit parameters are reported in Supporting Information.

As can be seen in Figure 3c,e,g, there was not a monotonic decrease in fluorescence with increasing depth. We attribute the noise to variations in hydrogel thickness, cross-sectional area, placement at the intended depth, and position relative to the excitation source. As illustrated by eq 11, variations in geometry and placement of the SWNT-gels necessarily change the signal by reducing the excitation power incident on the hydrogel and changing the attenuation distance of the excitation and fluorescence through tissue.

Although the penetration depth of the SWNT sensors in the target species were similar to that of previous studies,[62] the

DOI: 10.1021/acssensors.8b00538
ACS Sens. 2019, 4, 32−43

maximum depth can be increased using several approaches. First, the excitation and fluorescence detection equipment can be optimized specifically for SWNT-based biosensors. An InGaAs photodetector, which has almost an order of magnitude higher photoresponsivity (0.67 A/W at 1000 nm) may replace the silicon-based camera (0.067 A/W at 1000 nm) used in this study (Figure S-1). This equipment, along with other optical components such as lenses, can be attached directly to the animal instead of being placed at standoff distances, thus reducing the optical path length, optimizing excitation and fluorescence collection, and increasing signal. Alternatively, optical fibers may be implanted transdermally, in the form of an optode, to couple the excitation source directly with the hydrogel and the hydrogel with the photodetector.[68]

Ultimately, placement of the sensor could be influenced by other factors in addition to optical penetration depth, including local analyte concentration and sensor sensitivity. Many analytes of interest, such as glucose, cortisol, and vitamins, exist in interstitial fluids and can be theoretically queried with a hydrogel implanted superficially atop the hypodermis.[69]

Tissue Heterogeneity. Different color patterns of tissue and mechanically distinct exteriors may exist on the skin of the same animal, which may affect hydrogel implantation and/or fluorescence visibility. To examine this issue, we implanted hydrogels in different skin tissues of a juvenile female sea turtle (*Caretta caretta*) and a juvenile male blue shark (*Prionace glauca*). The sea turtle had both scaly and fleshy regions of the skin,[65] whereas the blue shark had distinctly colored regions ranging from dark blue to white.[70]

SWNT-gels were delivered in both the front right leg and the flesh centered underneath the neck of the sea turtle (Figure 4a,b). As the needle could not pierce the scales, it was inserted between them. The neck flesh was stretched prior to hydrogel placement to prevent folding of additional skin on top of the implant, avoiding artificial increases in the optical path length. The hydrogel was not visible beneath the scales but was visible beneath the fleshy skin of the neck (Figure 4c). SWNT-gel sensors were placed underneath the white and dark sections of shark's epidermis, and a nonfluorescent hydrogel was placed into a gray area to provide a baseline against which nIR fluorescent hydrogels could be compared (Figure 4d–f). The nIR fluorescent hydrogel was visible beneath the white but not the dark-colored epidermis (Figure 4g).

In both organisms, dark sections of tissue masked the nIR fluorescence of the sensor implants. Increased melanin levels in the epidermis result in higher absorption coefficients up to 1100 nm,[71,72] resulting in less excitation of the hydrogel and transmission of (6,5) SWNT fluorescence by increasing the values of γ_{ex} and γ_{em} in eq 11. UV–vis-NIR absorption measurements of tissue samples can quantify these wavelength/tissue dependent effects in a future study.

These results indicate two additional requirements for nIR fluorescent biosensors for *in vivo* applications. First, to maximize the signal-to-noise ratio, sensors should be delivered to tissues that are as optically transparent as possible for both the excitation and emission wavelengths. Furthermore, sensor fluorescence may have to be normalized against an invariant internal standard to eliminate the effects of tissue heterogeneity.[44] Second, to deliver hydrogels via a minimally invasive injection, some tissue sections will be inaccessible due to their mechanical strength and rigidity.

Imaging and Sensor Operation in Live Animals. Several questions regarding tolerance/biocompatibility of the implant and its effects on behavior can only be answered using living animals. A moving animal also adds greater complexity when imaging which may require reconfigurations of the sensor.

A female adult European eel (*Anguilla anguilla*), a female adult eastern river cooter (*Pseudemmys concinna*), and a juvenile male catshark (*Scyliorhinus stellaris*) were tagged with sensor hydrogels and monitored for up to 2 months. We attempted to image the eel and turtle in a small bucket from a distance of 0.5 m, but were unsuccessful for several reasons (Figure 5a–c). First, the camera and excitation sources were moved farther away to image the entire field of view. This reduced both the excitation power density incident upon the surface of the epidermis from 150 to 0.3 mW/cm^2 and consequently the fluorescence upon the camera's sensor by a factor of at least 500, according to eq 11. Furthermore, the combination of a long exposure time and animal movement apparently blurred the images.

Engineering Design for nIR Fluorescent Hydrogel Implants. A central goal of the current work is to utilize these findings to design sensing hydrogel implants. A wearable fluorescence reader that conforms to the animal's body as it moves is necessary.[73] Fixing the position of the measurement unit relative to the SWNT-gels eliminates changes in hydrogel fluorescence due to a changing excitation field and/or misalignment of the hydrogel and camera. Furthermore, placing the measurement device directly on top of the hydrogel reduces the optical path length, increasing the signal-to-noise ratio. As such, the miniaturization into and attachment methods of a flexible form factor are critical next steps.

Biocompatibility of the hydrogel was favorable in two of the three animals. We found no changes in movement or feeding behavior of the eel and catshark for two months post-implantation (Figure 5d). In the ultrasound images, the implantation site was identified via a slight change in tissue structure and echogenicity, but the surrounding tissue was completely normal (Figure 5e,f). In the case of a significant foreign body reaction, larger changes in architecture and echogenicity would be found in the periphery of the implant as it becomes encapsulated.[74,75] In contrast, histopathology suggested that the turtle experienced some reaction to the implant. The injection site did not heal cleanly (Figure 5g). It is important to note that there may have been an infection of the wound following implantation, precluding clean healing. Granules containing hydrogel fragments were extracted from the implantation site one month after the procedure (Figure 5h). H&E stained tissue sections showed infiltration of inflammatory cells into the deep dermis, hypodermis, and cutaneous muscle. The infiltrate consisted of heterophiles, macrophages, and several multinucleated giant cells, consistent with panniculitis and a foreign body reaction to the implant (Figure 5i). However, no behavioral changes were noted in the turtle.

A similar implantation procedure was performed on adult Sarasa comet goldfish (*Carassius auratus*), and its movement patterns were analyzed relative to a control goldfish without an implant (Figure 6a). Animal trajectories and position histograms did not differ significantly between the two animals, indicating that the hydrogel implants do not adversely impact animal health (Figure 6b–f). During times of stress or infections, the fish may swim violently or erratically. In the case of serious illness, fish movement would slow severely.[76,77] The video data and position histograms (Figure 6c–f) show that the subject fish showed neither erratic movement nor stationary behavior relative to the control. The absence of other abnormalities,

DOI: 10.1021/acssensors.8b00538
ACS Sens. 2019, 4, 32–43

such as damaged fins, disinterest in food, and discoloration, further indicate that the fish tolerated the implant well.[78] Furthermore, goldfish were maintained up to six months with the hydrogel implant, indicating long-term biocompatibility.

These results effectively form a pilot study that can be used to direct and prioritize future work involving larger sample sizes, a greater diversity of species, optimization of the hydrogel and delivery method, and development of a wearable fluorescence reader.

CONCLUSIONS

In summary, the feasibility of applying CoPhMoRe sensors for the physiological biologging of marine organisms was demonstrated in nine species of aquatic vertebrates. Future work will perform similar tissue penetration, tissue heterogeneity, and biocompatibility studies with a larger number of animals to probe phenotypic diversity. Strategies to normalize sensor signals against individual implant site optical properties and internal fluorescent standards will be explored to create absolute interspecies calibrations. Ratiometric approaches to optical sensing will mitigate movement and other artifacts that may confound the signal.[44] The successful measurement of the fluorescent hydrogels using an inexpensive, field portable Raspberry Pi imaging setup motivates further efforts to design a wearable, flexible sensor tag that integrates optoelectronic components tailored for physiological biologging using SWNT-gels. These technical improvements may improve the signal-to-noise ratio, time resolution of the measurements, and stability of the signal when attached to a moving animal. In parallel, the underlying SWNT nanosensors may be engineered to be sensitive to a wider range of bioanalytes to investigate a wider range of physiological states. The detection range of the riboflavin sensor described herein will be further improved to be sensitive to the physiologically relevant range. This work advances the application of biosensors into animals beyond the commonly used rodent and zebrafish models and carves a path toward the physiological biologging of aquatic organisms.

ASSOCIATED CONTENT

Supporting Information

The Supporting Information is available free of charge on the ACS Publications website at DOI: 10.1021/acssensors.8b00538.

Fit parameters for optical penetration depth model, comparison of SWNT fluorescence and photoresponsivity of common photodetectors (PDF)

AUTHOR INFORMATION

Corresponding Author

*E-mail: strano@mit.edu.

ORCID

Michael S. Strano: 0000-0003-2944-808X

Notes

The authors declare no competing financial interest.

ACKNOWLEDGMENTS

This research was supported by the King Abdullah University of Science & Technology (OSR-2015 Sensors 2707). FTN is supported by the Arnold and Mabel Beckman Foundation through the Arnold O. Beckman Postdoctoral Fellowship. The authors are also grateful to the Oceanogràfic animal care staff for performing animal handling, helpful discussions, and financial support (OCE-10-18) in performing this research. We also thank the Health and Animal Pathology Group, Dpt. PASAPTA, Facultad de Veterinaria, Universidad Cardenal Herrera-CEU, CEU Universities, for performing histological analysis and interpretation.

ABBREVIATIONS

SWNT, single wall carbon nanotube; CoPhMoRe, corona phase molecular recognition; nIR, near-infrared; PEGDA, poly(ethylene glycol) diacrylate; ss$(AC)_{15}$, single-stranded $(AC)_{15}$ DNA; InGaAs, Indium gallium arsenide

REFERENCES

(1) McIntyre, T. Trends in Tagging of Marine Mammals: A Review of Marine Mammal Biologging Studies. *African J. Mar. Sci.* **2014**, *36* (4), 409−422.

(2) Cooke, S. J.; Brownscombe, J. W.; Raby, G. D.; Broell, F.; Hinch, S. G.; Clark, T. D.; Semmens, J. M. Remote Bioenergetics Measurements in Wild Fish: Opportunities and Challenges. *Comp. Biochem. Physiol., Part A: Mol. Integr. Physiol.* **2016**, *202*, 23−37.

(3) Watanabe, Y. Y.; Ito, M.; Takahashi, A. Testing Optimal Foraging Theory in a Penguin−krill System. *Proc. R. Soc. London, Ser. B* **2014**, *281* (1779), 20132376.

(4) Amélineau, F.; Fort, J.; Mathewson, P. D.; Speirs, D. C.; Courbin, N.; Perret, S.; Porter, W. P.; Wilson, R. J.; Grémillet, D. Energyscapes and Prey Fields Shape a North Atlantic Seabird Wintering Hotspot under Climate Change. *R. Soc. Open Sci.* **2018**, *5*, 171883.

(5) Barnett, A.; Payne, N. L.; Semmens, J. M.; Fitzpatrick, R. Ecotourism Increases the Field Metabolic Rate of Whitetip Reef Sharks. *Biol. Conserv.* **2016**, *199*, 132−136.

(6) Baylis, A. M.M.; Orben, R. A.; Arnould, J. P.Y.; Peters, K.; Knox, T.; Costa, D. P.; Staniland, I. J. Diving Deeper into Individual Foraging Specializations of a Large Marine Predator, the Southern Sea Lion. *Oecologia* **2015**, *179* (4), 1053−1065.

(7) Hays, G. C.; Scott, R. Global Patterns for Upper Ceilings on Migration Distance in Sea Turtles and Comparisons with Fish, Birds and Mammals. *Funct. Ecol.* **2013**, *27* (3), 748−756.

(8) Yasuda, T.; Kawabe, R.; Takahashi, T.; Murata, H.; Kurita, Y.; Nakatsuka, N.; Arai, N. Habitat Shifts in Relation to the Reproduction of Japanese Flounder Paralichthys Olivaceus Revealed by a Depth-Temperature Data Logger. *J. Exp. Mar. Biol. Ecol.* **2010**, *385* (1−2), 50−58.

(9) Zhang, J.; Landry, M. P.; Barone, P. W.; Kim, J.-H.; Lin, S.; Ulissi, Z. W.; Lin, D.; Mu, B.; Boghossian, A. A.; Hilmer, A. J.; et al. Molecular Recognition Using Corona Phase Complexes Made of Synthetic Polymers Adsorbed on Carbon Nanotubes. *Nat. Nanotechnol.* **2013**, *8* (12), 959−968.

(10) Wu, D.; Sedgwick, A. C.; Gunnlaugsson, T.; Akkaya, E. U.; Yoon, J.; James, T. D. Fluorescent Chemosensors: The Past, Present and Future. *Chem. Soc. Rev.* **2017**, *46* (23), 7105−7123.

(11) Xiao, T.; Wu, F.; Hao, J.; Zhang, M.; Yu, P.; Mao, L. In Vivo Analysis with Electrochemical Sensors and Biosensors. *Anal. Chem.* **2017**, *89* (1), 300−313.

(12) Sun, W.; Guo, S.; Hu, C.; Fan, J.; Peng, X. Recent Development of Chemosensors Based on Cyanine Platforms. *Chem. Rev.* **2016**, *116* (14), 7768−7817.

(13) Soto, R. J.; Hall, J. R.; Brown, M. D.; Taylor, J. B.; Schoenfisch, M. H. In Vivo Chemical Sensors: Role of Biocompatibility on Performance and Utility. *Anal. Chem.* **2017**, *89* (1), 276−299.

(14) Rong, G.; Corrie, S. R.; Clark, H. A. In Vivo Biosensing: Progress and Perspectives. *ACS Sensors* **2017**, *2* (3), 327−338.

(15) Howes, P. D.; Chandrawati, R.; Stevens, M. M. Colloidal Nanoparticles as Advanced Biological Sensors. *Science (Washington, DC, U. S.)* **2014**, *346* (6205), 1247390.

DOI: 10.1021/acssensors.8b00538
ACS Sens. 2019, 4, 32−43

(16) Carter, K. P.; Young, A. M.; Palmer, A. E. Fluorescent Sensors for Measuring Metal Ions in Living Systems. *Chem. Rev.* **2014**, *114* (8), 4564−4601.
(17) Scholten, K.; Meng, E. A Review of Implantable Biosensors for Closed-Loop Glucose Control and Other Drug Delivery Applications. *Int. J. Pharm.* **2018**, *544* (2), 319−334.
(18) Cotruvo, J. A., Jr.; Aron, A. T.; Ramos-Torres, K. M.; Chang, C. J. Synthetic Fluorescent Probes for Studying Copper in Biological Systems. *Chem. Soc. Rev.* **2015**, *44* (13), 4400−4414.
(19) Sun, K.; Yang, Y.; Zhou, H.; Yin, S.; Qin, W.; Yu, J.; Chiu, D. T.; Yuan, Z.; Zhang, X.; Wu, C. Ultrabright Polymer-Dot Transducer Enabled Wireless Glucose Monitoring via a Smartphone. *ACS Nano* **2018**, *12* (6), 5176−5184.
(20) Deng, B.; Ren, M.; Kong, X.; Zhou, K.; Lin, W. Development of an Enhanced Turn-on Fluorescent HOCl Probe with a Large Stokes Shift and Its Use for Imaging HOCl in Cells and Zebrafish. *Sens. Actuators, B* **2018**, *255*, 963−969.
(21) Gurkov, A.; Sadovoy, A.; Shchapova, E.; Teh, C.; Meglinski, I.; Timofeyev, M. Microencapsulated Fluorescent PH Probe as Implantable Sensor for Monitoring the Physiological State of Fish Embryos. *PLoS One* **2017**, *12* (10), e0186548.
(22) Ferreira, N. R.; Ledo, A.; Laranjinha, J.; Gerhardt, G. A.; Barbosa, R. M. Simultaneous Measurements of Ascorbate and Glutamate in Vivo in the Rat Brain Using Carbon Fiber Nanocomposite Sensors and Microbiosensor Arrays. *Bioelectrochemistry* **2018**, *121*, 142−150.
(23) Mehrotra, P. Biosensors and Their Applications - A Review. *J. Oral Biol. Craniofacial Res.* **2016**, *6* (2), 153−159.
(24) Bisker, G.; Dong, J.; Park, H. D.; Iverson, N. M.; Ahn, J.; Nelson, J. T.; Landry, M. P.; Kruss, S.; Strano, M. S. Protein-Targeted Corona Phase Molecular Recognition. *Nat. Commun.* **2016**, *7*, 10241.
(25) Zhang, J. Q.; Boghossian, A. A.; Barone, P. W.; Rwei, A.; Kim, J. H.; Lin, D. H.; Heller, D. A.; Hilmer, A. J.; Nair, N.; Reuel, N. F.; et al. Single Molecule Detection of Nitric Oxide Enabled by d(AT)(15) DNA Adsorbed to Near Infrared Fluorescent Single-Walled Carbon Nanotubes. *J. Am. Chem. Soc.* **2011**, *133* (3), 567−581.
(26) Jin, H.; Heller, D. a; Kalbacova, M.; Kim, J.-H.; Zhang, J.; Boghossian, A. a; Maheshri, N.; Strano, M. S. Detection of Single-Molecule H2O2 Signalling from Epidermal Growth Factor Receptor Using Fluorescent Single-Walled Carbon Nanotubes. *Nat. Nanotechnol.* **2010**, *5* (4), 302−309.
(27) Kruss, S.; Landry, M. P.; Vander Ende, E.; Lima, B. M.A.; Reuel, N. F.; Zhang, J.; Nelson, J.; Mu, B.; Hilmer, A.; Strano, M. Neurotransmitter Detection Using Corona Phase Molecular Recognition on Fluorescent Single-Walled Carbon Nanotube Sensors. *J. Am. Chem. Soc.* **2014**, *136* (2), 713−724.
(28) Kruss, S.; Salem, D. P.; Vuković, L.; Lima, B.; Vander Ende, E.; Boyden, E. S.; Strano, M. S. High-Resolution Imaging of Cellular Dopamine Efflux Using a Fluorescent Nanosensor Array. *Proc. Natl. Acad. Sci. U. S. A.* **2017**, *114* (8), 1789−1794.
(29) Bisker, G.; Bakh, N. A.; Lee, M. A.; Ahn, J.; Park, M.; O'Connell, E. B.; Iverson, N. M.; Strano, M. S. Insulin Detection Using a Corona Phase Molecular Recognition Site on Single-Walled Carbon Nanotubes. *ACS Sensors* **2018**, *3* (2), 367−377.
(30) Iverson, N. M.; Barone, P. W.; Shandell, M.; Trudel, L. J.; Sen, S.; Sen, F.; Ivanov, V.; Atolia, E.; Farias, E.; McNicholas, T. P.; et al. In Vivo Biosensing via Tissue-Localizable near-Infrared-Fluorescent Single-Walled Carbon Nanotubes. *Nat. Nanotechnol.* **2013**, *8* (11), 873−880.
(31) Hays, G. C.; Ferreira, L. C.; Sequeira, A. M.M.; Meekan, M. G.; Duarte, C. M.; Bailey, H.; Bailleul, F.; Bowen, W. D.; Caley, M. J.; Costa, D. P.; et al. Key Questions in Marine Megafauna Movement Ecology. *Trends Ecol. Evol.* **2016**, *31* (6), 463−475.
(32) Payne, N. L.; Taylor, M. D.; Watanabe, Y. Y.; Semmens, J. M. From Physiology to Physics: Are We Recognizing the Flexibility of Biologging Tools? *J. Exp. Biol.* **2014**, *217* (3), 317−322.
(33) Wilson, R. P.; Gómez-Laich, A.; Sala, J. E.; Dell'Omo, G.; Holton, M. D.; Quintana, F. Long Necks Enhance and Constrain Foraging Capacity in Aquatic Vertebrates. *Proc. R. Soc. London, Ser. B* **2017**, *284* (1867), 20172072.
(34) Meekan, M. G.; Fuiman, L. A.; Davis, R.; Berger, Y.; Thums, M. Swimming Strategy and Body Plan of the World's Largest Fish: Implications for Foraging Efficiency and Thermoregulation. *Front. Mar. Sci.* **2015**, *2*, 64.
(35) Lee, M. A.; Bakh, N.; Bisker, G.; Brown, E. N.; Strano, M. S. A Pharmacokinetic Model of a Tissue Implantable Cortisol Sensor. *Adv. Healthcare Mater.* **2016**, *5* (23), 3004−3015.
(36) Pon, L. B.; Hinch, S. G.; Cooke, S. J.; Patterson, D. A.; Farrell, A. P. Physiological, Energetic and Behavioural Correlates of Successful Fishway Passage of Adult Sockeye Salmon Oncorhynchus Nerka in the Seton River, British Columbia. *J. Fish Biol.* **2009**, *74* (6), 1323−1336.
(37) Crossin, G. T.; Takahashi, A.; Sakamoto, K. Q.; Trathan, P. N.; Williams, T. D. Habitat Selection by Foraging Macaroni Penguins Correlates with Hematocrit, an Index of Aerobic Condition. *Mar. Ecol.: Prog. Ser.* **2015**, *530*, 163−176.
(38) O'Toole, A. C.; Dechraoui Bottein, M. Y.; Danylchuk, A. J.; Ramsdell, J. S.; Cooke, S. J. Linking Ciguatera Poisoning to Spatial Ecology of Fish: A Novel Approach to Examining the Distribution of Biotoxin Levels in the Great Barracuda by Combining Non-Lethal Blood Sampling and Biotelemetry. *Sci. Total Environ.* **2012**, *427−428*, 98−105.
(39) Kruss, S.; Hilmer, A. J.; Zhang, J.; Reuel, N. F.; Mu, B.; Strano, M. S. Carbon Nanotubes as Optical Biomedical Sensors. *Adv. Drug Delivery Rev.* **2013**, *65* (15), 1933−1950.
(40) Bisker, G.; Iverson, N. M.; Ahn, J.; Strano, M. S. A Pharmacokinetic Model of a Tissue Implantable Insulin Sensor. *Adv. Healthcare Mater.* **2015**, *4* (1), 87−97.
(41) Massey, V. The Chemical and Biological Versatility of Riboflavin. *Biochem. Soc. Trans.* **2000**, *28* (4), 283−296.
(42) Nakashima, N.; Okuzono, S.; Murakami, H.; Nakai, T.; Yoshikawa, K. DNA Dissolves Single-Walled Carbon Nanotubes in Water. *Chem. Lett.* **2003**, *32* (5), 456−457.
(43) Zheng, M.; Jagota, A.; Semke, E. D.; Diner, B. A.; McLean, R. S.; Lustig, S. R.; Richardson, R. E.; Tassi, N. G. DNA-Assisted Dispersion and Separation of Carbon Nanotubes. *Nat. Mater.* **2003**, *2* (5), 338−342.
(44) Giraldo, J. P.; Landry, M. P.; Kwak, S. Y.; Jain, R. M.; Wong, M. H.; Iverson, N. M.; Ben-Naim, M.; Strano, M. S. A Ratiometric Sensor Using Single Chirality Near-Infrared Fluorescent Carbon Nanotubes: Application to in Vivo Monitoring. *Small* **2015**, *11* (32), 3973−3984.
(45) Zhang, J.; Kruss, S.; Hilmer, A. J.; Shimizu, S.; Schmois, Z.; De La Cruz, F.; Barone, P. W.; Reuel, N. F.; Heller, D. A.; Strano, M. S. A Rapid, Direct, Quantitative, and Label-Free Detector of Cardiac Biomarker Troponin T Using Near-Infrared Fluorescent Single-Walled Carbon Nanotube Sensors. *Adv. Healthcare Mater.* **2014**, *3* (3), 412−423.
(46) Larsen, B. A.; Deria, P.; Holt, J. M.; Stanton, I. N.; Heben, M. J.; Therien, M. J.; Blackburn, J. L. Effect of Solvent Polarity and Electrophilicity on Quantum Yields and Solvatochromic Shifts of Single-Walled Carbon Nanotube Photoluminescence. *J. Am. Chem. Soc.* **2012**, *134* (30), 12485−12491.
(47) Choi, J. H.; Strano, M. S. Solvatochromism in Single-Walled Carbon Nanotubes. *Appl. Phys. Lett.* **2007**, *90* (22), 88−91.
(48) Tokarev, I.; Minko, S. Stimuli-Responsive Porous Hydrogels at Interfaces for Molecular Filtration, Separation, Controlled Release, and Gating in Capsules and Membranes. *Adv. Mater.* **2010**, *22* (31), 3446−3462.
(49) Zhao, F.; Yao, D.; Guo, R.; Deng, L.; Dong, A.; Zhang, J. Composites of Polymer Hydrogels and Nanoparticulate Systems for Biomedical and Pharmaceutical Applications. *Nanomaterials* **2015**, *5* (4), 2054−2130.
(50) Peppas, N. A.; Huang, Y.; Torres-Lugo, M.; Ward, J. H.; Zhang, J. Physicochemical Foundations and Structural Design of Hydrogels in Medicine and Biology. *Annu. Rev. Biomed. Eng.* **2000**, *2* (1), 9−29.
(51) Peppas, N. A.; Hilt, J. Z.; Khademhosseini, A.; Langer, R. Hydrogels in Biology and Medicine: From Molecular Principles to Bionanotechnology. *Adv. Mater.* **2006**, *18* (11), 1345−1360.

DOI: 10.1021/acssensors.8b00538
ACS Sens. 2019, 4, 32−43

(52) Pedersen, J. S.; Sommer, C. Temperature Dependence of the Virial Coefficients and the Chi Parameter in Semi-Dilute Solutions of PEG. *Prog. Colloid Polym. Sci.* **2005**, *130*, 70−78.
(53) Hays, G. C.; Bastian, T.; Doyle, T. K.; Fossette, S.; Gleiss, A. C.; Gravenor, M. B.; Hobson, V. J.; Humphries, N. E.; Lilley, M. K.S.; Pade, N. G.; et al. High Activity and Levy Searches: Jellyfish Can Search the Water Column like Fish. *Proc. R. Soc. London, Ser. B* **2012**, *279* (1728), 465−473.
(54) Göröcs, Z.; Rivenson, Y.; Ceylan Koydemir, H.; Tseng, D.; Troy, T. L.; Demas, V.; Ozcan, A. Quantitative Fluorescence Sensing Through Highly Autofluorescent, Scattering, and Absorbing Media Using Mobile Microscopy. *ACS Nano* **2016**, *10* (9), 8989−8999.
(55) Lim, C.; Leamaster, B.; Brock, J. A. Riboflavin Requirement of Fingerling Red Hybrid Tilapia Grown in Seawater. *J. World Aquacult. Soc.* **1993**, *24* (4), 451−458.
(56) Petteys, B. J.; Frank, E. L. Rapid Determination of Vitamin B2 (Riboflavin) in Plasma by HPLC. *Clin. Chim. Acta* **2011**, *412* (1), 38−43.
(57) Yao, Y.; Yonezawa, A.; Yoshimatsu, H.; Omura, T.; Masuda, S.; Matsubara, K. Involvement of Riboflavin Transporter RFVT2/Slc52a2 in Hepatic Homeostasis of Riboflavin in Mice. *Eur. J. Pharmacol.* **2013**, *714* (1), 281−287.
(58) Bashkatov, A. N.; Genina, E. A.; Kochubey, V. I.; Tuchin, V. V. Optical Properties of Human Skin, Subcutaneous and Mucous Tissues in the Wavelength Range from 400 to 2000 Nm. *J. Phys. D: Appl. Phys.* **2005**, *38* (15), 2543−2555.
(59) Smith, A. M.; Mancini, M. C.; Nie, S. Bioimaging: Second Window for in Vivo Imaging. *Nat. Nanotechnol.* **2009**, *4*, 710−711.
(60) Welsher, K.; Liu, Z.; Sherlock, S. P.; Robinson, J. T.; Chen, Z.; Daranciang, D.; Dai, H. A Route to Brightly Fluorescent Carbon Nanotubes for Near-Infrared Imaging in Mice. *Nat. Nanotechnol.* **2009**, *4* (11), 773−780.
(61) Luo, S.; Zhang, E.; Su, Y.; Cheng, T.; Shi, C. A Review of NIR Dyes in Cancer Targeting and Imaging. *Biomaterials* **2011**, *32* (29), 7127−7138.
(62) Iverson, N. M.; Bisker, G.; Farias, E.; Ivanov, V.; Ahn, J.; Wogan, G. N.; Strano, M. S. Quantitative Tissue Spectroscopy of near Infrared Fluorescent Nanosensor Implants. *J. Biomed. Nanotechnol.* **2016**, *12* (5), 1035−1047.
(63) Hawkes, J. W. The Structure of Fish Skin. *Cell Tissue Res.* **1974**, *149* (713), 147−158.
(64) Jordan, T. M.; Partridge, J. C.; Roberts, N. W. Non-Polarizing Broadband Multilayer Reflectors in Fish. *Nat. Photonics* **2012**, *6* (11), 759−763.
(65) Spotila, J. R. *Sea Turtles: A Complete Guide to Their Biology, Behavior, and Conservation*; Johns Hopkins University Press: Baltimore, 2004.
(66) Ng, K.-C. C.; Ooi, A.-C. P. A Review of Fish Taxonomy Conventions and Species Identification Techniques. *J. Surv. Fish. Sci.* **2017**, *4* (1), 54−93.
(67) Human, B. A.; Owen, E. P.; Compagno, L. J. V.; Harley, E. H. Testing Morphologically Based Phylogenetic Theories within the Cartilaginous Fishes with Molecular Data, with Special Reference to the Catshark Family (Chondrichthyes; Scyliorhinidae) and the Interrelationships within Them. *Mol. Phylogenet. Evol.* **2006**, *39* (2), 384−391.
(68) Kosoglu, M. A.; Hood, R. L.; Chen, Y.; Xu, Y.; Rylander, M. N.; Rylander, C. G. Fiber Optic Microneedles for Transdermal Light Delivery: Ex Vivo Porcine Skin Penetration Experiments. *J. Biomech. Eng.* **2010**, *132* (9), 91014−91017.
(69) Matzeu, G.; Florea, L.; Diamond, D. Advances in Wearable Chemical Sensor Design for Monitoring Biological Fluids. *Sens. Actuators, B* **2015**, *211*, 403−418.
(70) Allaby, M. Carcharhinidae. In *A Dictionary of Zoology*; Oxford University Press, 2009.
(71) Jacques, S. L. Optical Properties of Biological Tissues: A Review. *Phys. Med. Biol.* **2013**, *58* (11), R37−R61.
(72) Anderson, R. R.; Parrish, J. A. The Optics of Human Skin. *J. Invest. Dermatol.* **1981**, *77* (1), 13−19.
(73) Nassar, J. M.; Khan, S. M.; Velling, S. J.; Diaz-Gaxiola, A.; Shaikh, S. F.; Geraldi, N. R.; Torres Sevilla, G. A.; Duarte, C. M.; Hussain, M. M. Compliant Lightweight Non-Invasive Standalone "Marine Skin" Tagging System. *npj Flex. Electron.* **2018**, *2* (1), 13.
(74) Ando, A.; Hatori, M.; Hagiwara, Y.; Isefuku, S.; Itoi, E. Imaging Features of Foreign Body Granuloma in the Lower Extremities Mimicking a Soft Tissue Neoplasm. *Upsala J. Med. Sci.* **2009**, *114* (1), 46−51.
(75) Anderson, J. M.; Rodriguez, A.; Chang, D. T. Foreign Body Reaction to Biomaterials. *Semin. Immunol.* **2008**, *20* (2), 86−100.
(76) Adelman, J. S.; Martin, L. B. Vertebrate Sickness Behaviors: Adaptive and Integrated Neuroendocrine Immune Responses. *Integr. Comp. Biol.* **2009**, *49* (3), 202−214.
(77) Ashley, P. J.; Sneddon, L. U. Pain and Fear in Fish. In *Fish Welfare*; Branson, E. J., Ed.; Blackwell, 2008; 49−77.
(78) Stoskopf, M. K. Biology and Management of Laboratory Fishes. In *Laboratory Animal Medicine*, Anderson, L. C.; Otto, G. M.; Pritchett-Corning, K. R.; Whary, M. T. B. T., Eds.; Academic Press: Boston, 2015; pp 1063−1086.

DOI: 10.1021/acssensors.8b00538
ACS Sens. 2019, 4, 32−43